Multifaceted cancer alleviation by cowpea mosaic virus in a bioprinted ovarian cancer peritoneal spheroid model

Yi Xiang [a,1], Zhongchao Zhao [a,b,c,1], Emmie J. Yao [a], Alis Balayan [a,d], Steven N. Fiering [e,f], Nicole F. Steinmetz [a,b,c,g,h,i,j,k,**], Shaochen Chen [a,b,h,i,*]

[a] Aiiso Yufeng Li Family Department of Chemical and Nano Engineering, University of California, San Diego, 9500 Gilman Dr., La Jolla, CA, 92093, USA
[b] Center for Nano-ImmunoEngineering, University of California, San Diego, 9500 Gilman Dr., La Jolla, CA, 92093, USA
[c] Moores Cancer Center, University of California, San Diego, 9500 Gilman Dr., La Jolla, CA, 92093, USA
[d] School of Medicine, University of California, San Diego, 9500 Gilman Dr., La Jolla, CA, 92093, USA
[e] Department of Microbiology and Immunology, Geisel School of Medicine at Dartmouth, Lebanon, NH, 03756, USA
[f] Dartmouth Cancer Center, Geisel School of Medicine at Dartmouth and Dartmouth Health, Lebanon, NH, 03756, USA
[g] Department of Radiology, University of California, San Diego, 9500 Gilman Dr., La Jolla, CA, 92093, USA
[h] Shu Chien-Gene Lay Department of Bioengineering, University of California, San Diego, 9500 Gilman Dr., La Jolla, CA, 92093, USA
[i] Institute for Materials Discovery and Design, University of California, San Diego, 9500 Gilman Dr., La Jolla, CA, 92093, USA
[j] Center for Engineering in Cancer, University of California, San Diego, 9500 Gilman Dr., La Jolla, CA, 92093, USA
[k] Shu and K.C. Chien and Peter Farrell Collaboratory, University of California, San Diego, 9500 Gilman Dr., La Jolla, CA, 92093, USA

ARTICLE INFO

ABSTRACT

Ovarian cancer (OvCa) is a leading cause of mortality among gynecological malignances and usually manifests as intraperitoneal spheroids that generate metastases, ascites, and an immunosuppressive tumor microenvironment. In this study, we explore the immunomodulatory properties of cowpea mosaic virus (CPMV) as an adjuvant immunotherapeutic agent using an in vitro model of OvCa peritoneal spheroids. Previous findings highlighted the potent efficacy of intratumoral CPMV against OvCa in mouse tumor models. Leveraging the precision control over material deposition and cell patterning afforded by digital-light-processing (DLP) based bioprinting, we constructed OvCa-macrophage spheroids to mimic peritoneal spheroids using gelatin methacrylate (GelMA), a collagen-derived photopolymerizable biomaterial to mimic the extracellular matrix. Following CPMV treatment, bioprinted spheroids exhibited inhibited OvCa progression mediated by macrophage activation. Our analysis indicates that CPMV regulates and activates macrophage to both induce OvCa cell killing and restore normal cell-cell junctions. This study deepened our understanding of the mechanism of CPMV intratumoral immunotherapy in the setting of OvCa. This study also highlights the potential of studying immunotherapies using high throughput tissue models via DLP bioprinting.

1. Introduction

Ovarian cancer (OvCa) is the most lethal gynecological malignancy worldwide [1]. Its mortality stems from late diagnosis, high metastatic potential, high recurrence rate following surgery and chemotherapy, chemoresistance and tumor heterogeneity. A significant contributor to the high mortality of the epithelial ovarian cancer is its unique dissemination mechanism, which results from the formation of aggregates of malignant cells, often referred to as spheroids [2]. These spheroids play a pivotal role in transcoelomic metastasis, causing widespread dissemination and associated ascites. Intercellular interactions within the spheroids, especially between OvCa cells and tumor-associated macrophages, further contribute to the progression of the malignancy [3] by fostering an immunosuppressive tumor

---

microenvironment (TME) and leading to chemoresistance.

Cowpea mosaic virus (CPMV) is a non-enveloped plant virus that self-assembles into icosahedral nucleoprotein assemblies that are 30 nm-sized nanoparticles. Due to its immunostimulatory nature, intratumoral CPMV generates potent and durable anti-tumor immune efficacy against solid tumors. This was demonstrated in multiple tumor mouse models [4] and canine cancer patients [5]. Notably, CPMV can suppress tumor growth in the highly aggressive and non-immunogenic murine ID8/Defb29/Vegf-A-Luc ovarian cancer model [6,7], in which transcoelomic spheroids predominantly comprised of OvCa cells and macrophages have been observed and characterized [8]. Therefore, CPMV is a promising candidate for OvCa immunotherapy. Deeper understanding of CPMV mediated anti-tumor immunity against OvCa could pave the way for a clinically translatable adjuvant immunotherapy for ovarian cancer.

Previous studies have shown that CPMV primes anti-tumor immunity through engagement and activation of the innate immune system which ultimately primes adaptive anti-tumor immunity [9]. It has been established that ID8/Defb29/Vegf-A-Luc cells could be inhibited by RAW264.7 macrophages pulsed with CPMV in a conventional *in vitro* co-culture experiment [6]. Given that both OvCa cell and macrophages are crucial components of the transcoelomic spheroids, we hypothesize that CPMV could mitigate the malignancy of OvCa spheroids through macrophage activation. Thus, we investigated the immunomodulatory properties of CPMV in OvCa spheroids.

In vitro OvCa spheroids have been developed using a variety of cell sources, biomaterials and biofabrication strategies [10–13]. Essentially, when OvCa cells and macrophages are co-cultured in a 3D environment, spheroids spontaneously form as the cells aggregate, reorganize, and differentiate. In this study, we utilize digital-light-processing (DLP)
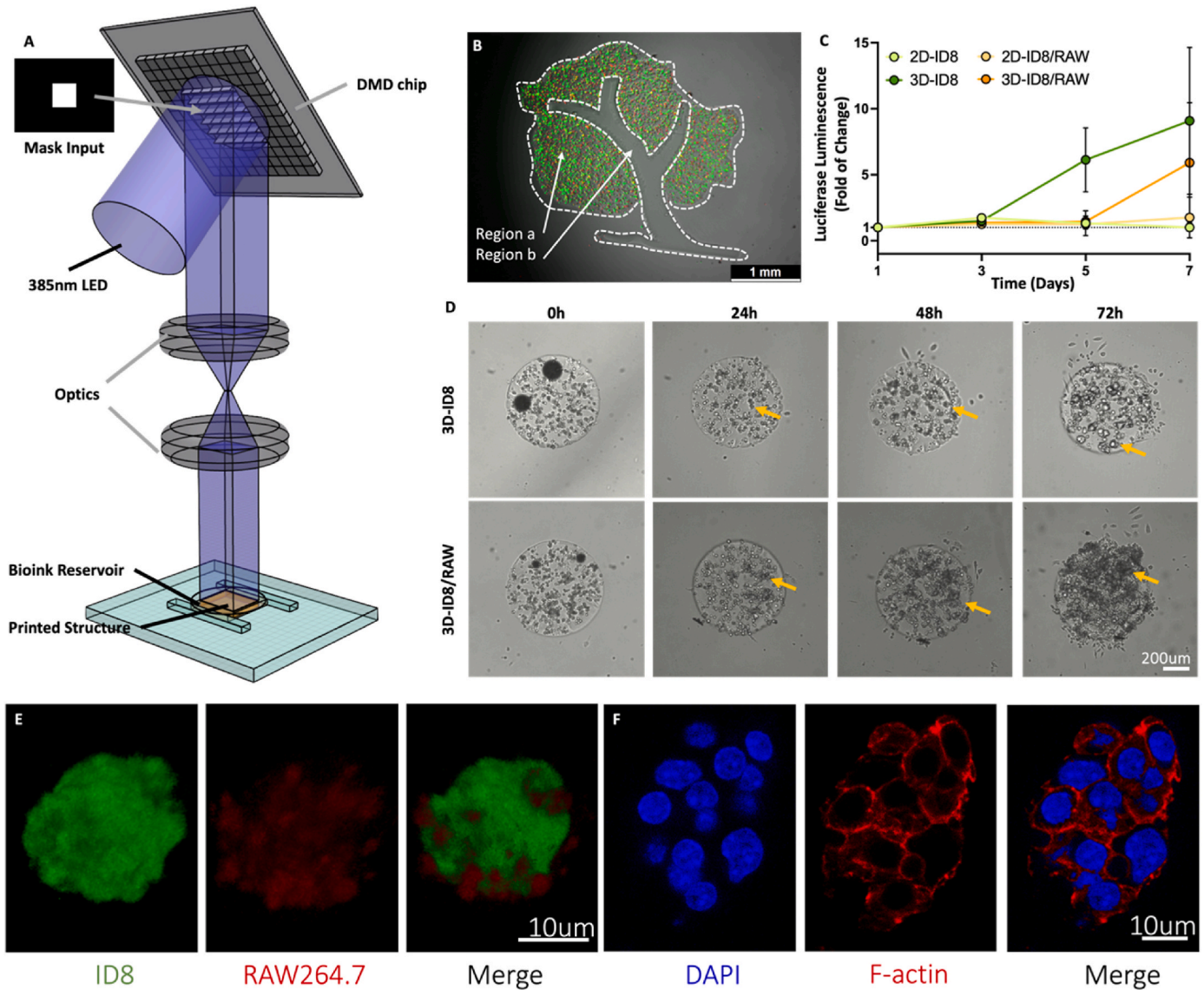

Fig. 1. OvCa-Mac model was constructed by DLP bioprinting to recapitulate the peritoneal spheroids in OvCa progression. A. Schematic of the DLP bioprinting set-up. B. A sample print of ID8/RAW co-culture in an ovarian solid tumor mimicking scaffold. Region a: cellular part mimicking solid tumor, Green: ID8, Orange: RAW; region b: acellular part for potential incorporation of further tumor microenvironment components. C. Growth profile of ID8 and ID8/RAW co-culture in the bioprinted 3D scaffold and in conventional 2D culture setting; the growth profile was measured based on Luciferase expression using Luc-expressing ID8/Defb29/Vegf-A-Luc cells. D. Brightfield images of ID8 and ID8/RAW in the bioprinted 3D scaffold from 0 h (as printed) to 72hr (spheroids formed and migration observed). E. 3D reconstruction of cell reorganization in an ID8/RAW spheroid in a bioprinted scaffold. Green: ID8, Red: RAW264.7. Scale bar: 10 μ m. F. F-actin and nuclei co-localization of an ID8/RAW spheroid in a bioprinted scaffold. Blue: nuclei (DAPI), Red: F-actin (Phalloidin). (For interpretation of the references to color in this figure legend, the reader is referred to the Web version of this article.)

based bioprinting, which allows for controlled photopolymerization, to create cell-encapsulating hydrogel scaffolds with a controlled shape, size, initial cell count, and mechanical properties [14]. Gelatin methacrylate (GelMA) is used as the matrix material for the scaffold.

Originating from collagen I, GelMA models the extracellular matrix (ECM) to which OvCa cells preferentially adhere. The methacrylate functional groups of GelMA enable a controllable and highly reproducible 3D bioprinting process. Here, we established DLP-bioprinted OvCa-macrophage spheroids and subjected them to CPMV treatment. This innovative application of GelMA in conjunction with DLP bioprinting for OvCa modeling allows us to recapitulate the immunosuppressive tumor microenvironment more accurately. By leveraging the unique properties of GelMA, we enhance the structural and functional fidelity of our in vitro OvCa models. We evaluated the inhibition of OvCa spheroid growth by macrophages activated with CPMV. We investigated the role of CPMV in regulating the primary mechanisms through which macrophages directly interact and affect cancer cells. Additionally, we assessed how CPMV treatment alters the OvCa-macrophage interactions and its potential impact on OvCa progression. This study advances our understanding of CPMV's mechanisms of action on macrophages and ultimately tumor cells. Furthermore, our results validate the DLP bioprinting approach for the development of clinically relevant tissue models to study immunotherapy.

2. Results

2.1. OvCa-mac model construction

Throughout all studies, the ID8/Defb29/Vegf-A-Luc and RAW264.7 cell lines were used and will be referred to as ID8 and RAW, respectively. A 3D ID8/RAW co-culture scaffold based on GelMA was bioprinted with an in-house developed DLP bioprinter [15], designed to support *in situ* formation of OvCa-macrophage (OvCa-Mac) spheroids. As illustrated in Fig. 1A, a user-defined mask confines the light irradiation of the bioink reservoir and dictates the pattern of the scaffold. Exposure time is rationally controlled to achieve a designated stiffness (Fig. S1). After printing, both types of cells are encapsulated in GelMA, and they proliferate, interact, migrate, aggregate, and reorganize (Fig. 1B, region a). The fine resolution of the bioprinting system (~5 μm) allowed us to create more intricate structures, such as the ovarian solid tumor mimicking shape shown in Fig. 1B. In this model, additional TME components, such as vasculature, epithelium, or void space for immune cell perfusion, could eventually be incorporated in region b.

The formation of the OvCa-Mac spheroid was initially assessed by the cell growth profile. Specifically, we used luciferase-expressing ID8/Defb29/Vegf-A-Luc cells which enabled monitoring of cell proliferation based on increased luciferase expression. As shown in Fig. 1C, both ID8 and ID8/RAW in 3D scaffolds proliferated throughout the 7 days of culture. In contrast, in the traditional 2D culture, the growth of ID8 in both ID8-only and ID8/RAW scaffolds plateaued after they reached confluency on day 3.

Brightfield images in Fig. 1D revealed the emergence of the spheroids (annotated by arrows) in the ID8 scaffolds starting from 24 h postprinting, which is even more pronounced in the ID8/RAW scaffolds. With extended culture time, both the size and number of these spheroids increased (Fig. S2). Notably, compared to the ID8-only scaffolds, the spheroids in ID8/RAW scaffolds were larger by 48 h and displayed enhanced migration out of the spheroid by 72 h.

The spheroids' organization were further investigated by confocal imaging. Fig. 1E presents a 3D reconstruction of a spheroid, in which ID8 was labeled with CellTracker Green and RAW was labeled with CellTracker Orange. It shows that the two types of cells were organized in an intertwined arrangement to a diameter of approximately 30 μm, and RAW cells were observed both on the surface and in the center of the spheroid. Cytoskeleton and nuclei distribution in the spheroid was revealed by Fig. 1F, underscoring a densely packed, multicellular

assembly comprised of cells of varied sizes.

2.2. Evaluation of OvCA-Mac model response to CPMV treatment

ID8/RAW (scaffolds of ID8 cells and RAW cells) were printed with an ID8:RAW ratio of 1:1. After incubation under normal cell culture conditions for 48 h when spheroids had appeared the various scaffolds received CPMV or sham treatment to investigate how the system responded to this treatment. CPMV-treated scaffolds received 10 μg CPMV added per scaffold in fresh media and sham-treated scaffolds received only added fresh media (Fig. 2Ai). ID8/CPMV (scaffolds with only ID8 cells, treated with CPMV) and ID8/sham scaffolds served as controls to delineate the direct impact of CPMV on OvCa cells. ID8/SUP scaffolds were ID8-only scaffolds treated with supernatant from RAW/CPMV (referred to as ID8/SUP/CPMV) or supernatant from RAW/sham (referred to as ID8/SUP/sham) scaffolds to examine the effect on ID8-only scaffolds of the paracrine secretion of RAW due to CPMV stimulation (Fig. 2Aii). A table of the nomenclature of all the conditions discussed is provided in Table S1.

The treatment response was first evaluated by luciferase bioluminescence which reflects the number of viable ID8 cells. As shown in Fig. 2B–a significant decrease (P < 0.05*) in the bioluminescence of ID8 cells was induced by CPMV in the ID8/RAW and ID8/SUP scaffolds, which mirrored the CPMV-stimulated OvCa inhibition observed in previous animal studies [6]. In contrast, no change occurred in ID8-only CPMV-exposed scaffolds indicating that ID8 is not directly affected by CPMV. This data supports the conclusion that macrophages play a key role in CPMV-mediated anti-tumor efficacy.

Macrophages can directly inhibit cancer cells mainly through three major mechanisms – nitric oxide (NO) production, TNF-α protein production, and phagocytosis. Therefore, the OvCa-Mac model response was further investigated by assaying transcription of relevant genes. A comprehensive set of phagocytosis associated genes [16] was quantified by qPCR, and the fold change was compared between ID8/RAW/CPMV vs. ID8/RAW/sham and RAW/CPMV vs. RAW/sham (Fig. 2C). In RAW/CPMV scaffolds, upregulation of genes associated with SCAR/WAVE complex (NCKAP, ABI1), ARP2/3 complex (ARPC2, ACTR2), and Ragulator target RRAGA was observed, compared to the RAW/sham scaffolds. Furthermore, RAC1, a gene related to phagocytic cup formation, was increased, while DOCK2, another gene with the same function, was downregulated. Expression of LAMTOR2, a mTOR-associated member of the lysosomal Ragulator complex, was also suppressed. Overall, there was an upregulation trend in the expression of phagocytosis-associated genes due to CPMV treatment, suggesting enhanced RAW phagocytosis. In ID8/RAW/CPMV scaffolds, there was also a prominent upregulation of the phagocytosis-related genes. Notably, RAC1 and DOCK2 were both increased, and LAMTOR2 remained unchanged compared to ID8/RAW/sham. Other genes in the panel were all upregulated and exhibited greater fold increase than those in RAW-only scaffolds. Overall, the ID8/RAW/CPMV scaffolds demonstrated a notable upregulation in phagocytosis-related genes, with a more pronounced increase compared to RAW-only scaffolds, highlighting CPMV's role in enhancing phagocytic gene expression.

Increased phagocytosis of RAW was further investigated and quantified in terms of CPMV uptake and ID8 engulfment using a flow cytometry-based assay (Fig. 2D) [17]. To carry out this experiment, we synthesized Cy5 conjugated CPMV (CPMV-Cy5) using a previously established protocol [18,19]. The success of Cy5 conjugation to CPMV was confirmed by native agarose gel electrophoresis and denatured SDS-PAGE with the co-migration of Cy5 fluorescence, CPMV RNA, and protein (Figs. S3A and B). Assaying by UV–Vis spectrophotometry, ~30 Cy5 molecules were attached per CPMV (Fig. S3C). DLS and TEM analysis showed that CPMV-Cy5 maintained a similar size and virus structure to native CPMV (Figs. S3D and E). ID8 cells were labeled with CellTracker Green prior to bioprinting. After incubating with CPMV-Cy5 for 24 h, 45.70 ± 4.757 % of RAW cells in the ID8RAW/CPMV scaffolds,
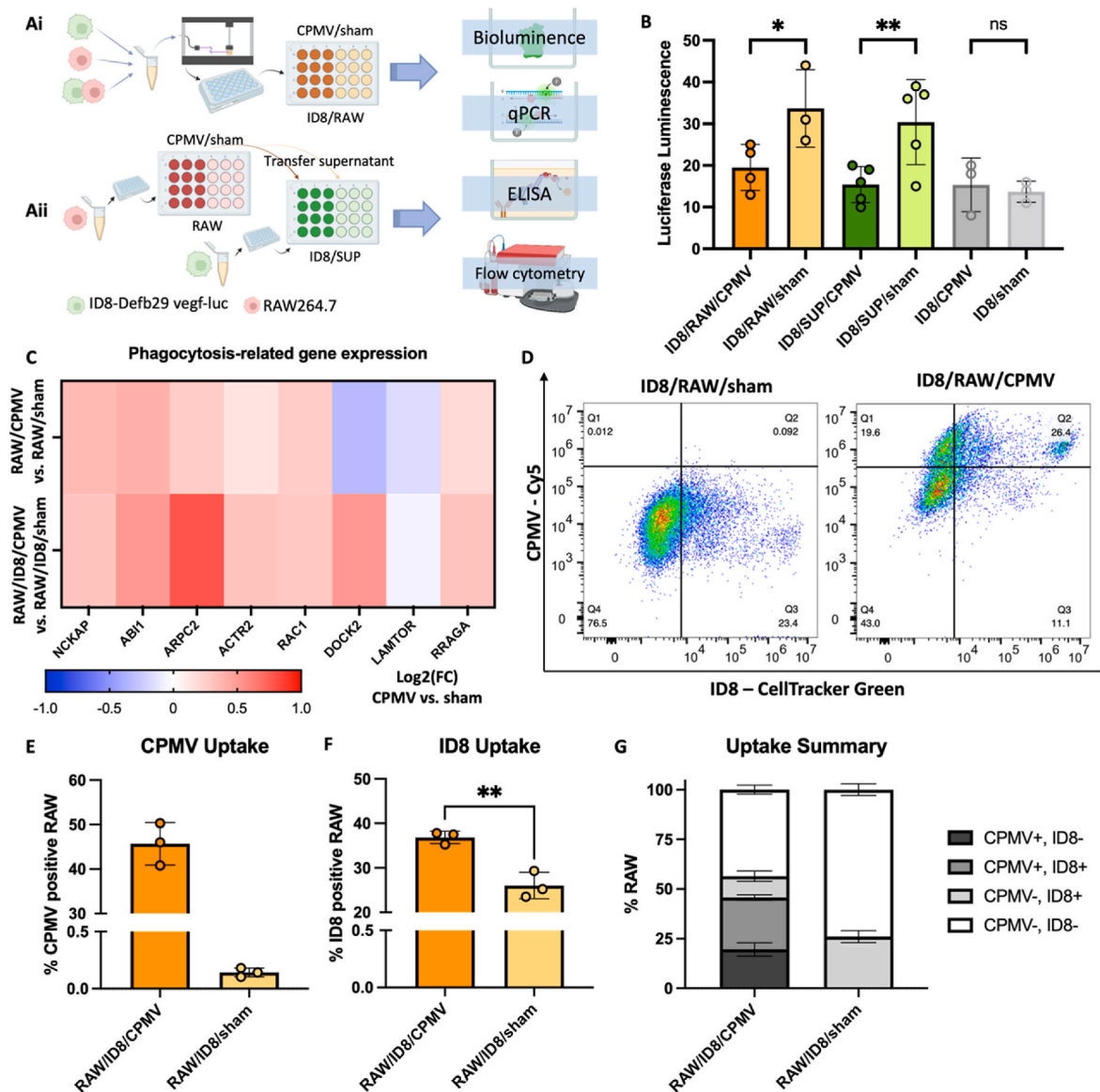
Fig. 2. CPMV stimulates RAW to inhibit ID8 by enhancing phagocytosis. A. Illustration of sample preparation and CPMV treatment process of each condition. i. ID8/RAW/CPMV and ID8/RAW/sham; ii. RAW/CPMV, RAW/sham, ID8/SUP/CPMV, ID8/SUP/sham. B. ID8 cell bioluminescence was inhibited by CPMV in ID8/RAW dual cell spheroids and supernatant of CPMV-treated RAW cells, but not direct treatment of CPMV. C. mRNA expression of phagocytosis-related genes was upregulated upon CPMV treatment, quantified by qPCR. D. RAW264.7 engulfment of ID8 was enhanced by CPMV uptake, quantified by flow cytometry-based phagocytosis assay. (Left: ID8/RAW/sham; Right: ID8/RAW/CPMV) Statistics of CPMV uptake, ID8 uptake and overall uptake were summarized in E, F, and G, respectively. (*P < 0.05, **P < 0.01).

labeled by PE/Cy5 conjugated F4/80 antibody prior to flow cytometry, are positive for Cy5, suggesting substantial uptake of CPMV by RAW cells (Fig. 2E). ID8 uptake was observed in both ID8/RAW/CPMV and ID8/RAW/sham scaffolds, as characterized by the appearance of Cell-Tracker Green signal in RAW cells, with a significant increase when the scaffolds were treated with CPMV (Fig. 2F, P < 0.01**). The CPMV-stimulated uptake of ID8 was also suggested by a notable population of CPMV$^+$, ID8$^+$ RAWs (Fig. 2D and G) of 26.1 ± 1.37 %.

The gene profiling is consistent with CPMV stimulating OvCa cell engulfment by macrophages. However, that does not rule out paracrine mechanisms since the number of live ID8 cells by luciferase also significantly decreased when the ID8 scaffolds were treated with RAW/CPMV supernatant, compared to the scaffolds treated with RAW/sham supernatant (Fig. 2B, P < 0.01**). This suggests that secretions from the RAW cells were affecting ID8. Therefore, the production of nitric oxide and TNF-α protein was investigated. While changes in nitric oxide

production were not observed (Fig. S4), a significant increase in TNF-α protein secretion was observed in both RAW/CPMV (compared to RAW/sham, P < 0.05*) and ID8/RAW/CPMV (compared to ID8/RAW/sham, P < 0.05*), as quantified by ELISA (Fig. 3A). It was also notable that more TNF-α protein was observed in ID8/RAW scaffolds than RAW scaffolds, while ID8 scaffolds did not produce TNF-α protein regardless of CPMV treatment. The TNF pathway plays a complex role in cell fate. While TNF-α can induce apoptosis through activation of caspase 8 and caspase 3, it can also lead to inflammation and survival through alternative activation via TRAF2 and activated MAPK and NF-κB pathways (Fig. 3B). Therefore, we investigated the gene expression of apoptosis activation and alternative activation, respectively.

As shown in Fig. 3C, treatment of CPMV increased TNF, CASP8, CASP3 gene expression in ID8/RAW/CPMV compared to ID8/RAW/sham, but not in ID8/CPMV compared to ID8/sham, as measured by qPCR quantification of mRNA. This suggests that CPMV activates TNF-α
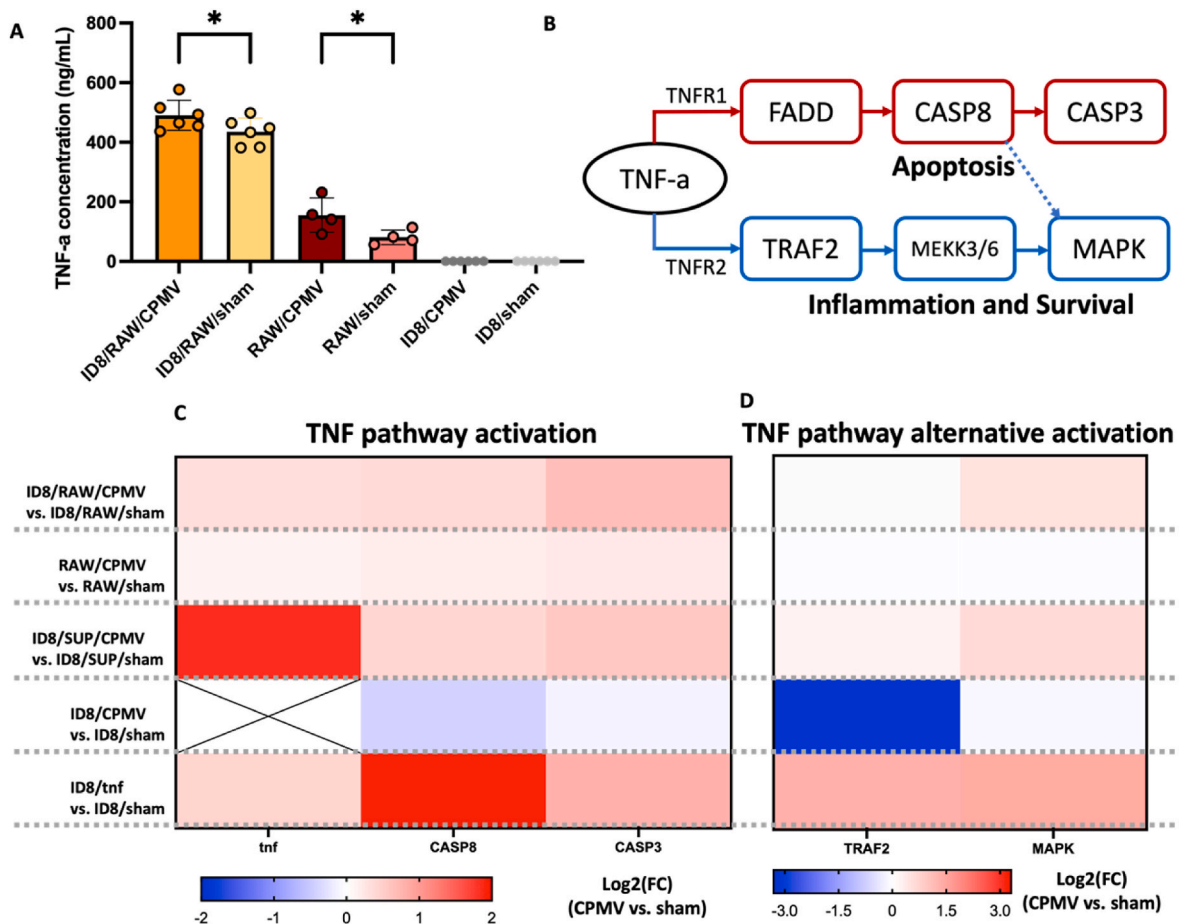
Fig. 3. CPMV induced ID8 apoptosis through RAW by mediating TNF pathway activation. A. TNF-α produced by ID8/RAW spheroids, RAW and ID8 quantified by ELISA. B. Schematic of TNF pathway activation. Relative mRNA expression of TNF-activated apoptosis related genes (C) and alternative activation related genes (D), quantified by qPCR. (*P < 0.05).

induced apoptosis through CPMV impact on RAW. These genes were also upregulated in RAW-only scaffolds upon CPMV treatment. Notably, we observe a clear increase in TNF expression in the ID8/SUP/CPMV group as well as in the ID8/tnf scaffolds (ID8 scaffold treated with an equivalent amount of TNF-α protein as produced by the RAW/CPMV scaffolds). However, the elevation of TNF mRNA was not as pronounced in ID8/RAW/CPMV where ID8 and RAW cells were co-cultured. This indicates that the direct interaction between ID8 and RAW cells modulates TNF expression differently compared to treatment with RAW/CPMV supernatant alone.

The ID8/tnf also showed a higher upregulation of CASP8 expression and a lower upregulation of CASP3 compared to ID8/SUP/CPMV, pointing out that the RAW/CPMV supernatant treatment had a stronger apoptotic induction than the TNF-α protein treatment.

Regarding alternative TNF activation pathway, no change in TRAF2 expression was shown in the ID8/RAW/CPMV and RAW/CPMV compared to their sham. Slight upregulation of MAPK was observed in ID8/RAW/CPMV but not RAW/CPMV. While being a regulatory target of alternative TNF activation, MAPK is also involved in a number of signal transduction pathways. The increase here could be a result of other stimulatory effects of the CPMV treatment. On the other hand, ID8/SUP/CPMV scaffolds went through a slight upregulation of TRAF2 and MAPK, and a more notable increase of both genes was observed in ID8 scaffolds treated by the TNF-α protein, while a downregulation of TRAF2 of 3-fold was observed in ID8 scaffolds treated with CPMV. These results suggested that in addition to the apoptosis activation, alternative TNF pathway activation in ID8 scaffolds was also initiated by the paracrine secretion from RAW cells when stimulated by CPMV, but not

directly by CPMV. Compared to TNF-α protein treatment, RAW/CPMV supernatant treatment with a similar level of TNF-α protein led to a weaker alternative activation while it also showed stronger apoptotic activation. The production, metabolism or signaling role of TNF-α stimulated by CPMV was also modified in ID8/RAW as compared to ID8/SUP/CPMV scaffolds.

2.3. Macrophage activation

Since production of TNF-α is a major marker of inflammatory polarization of macrophages, the M1/M2 polarization biomarker gene expression levels were also quantified in the ID8/RAW and RAW-only scaffolds. However, the data turned out inconclusive of a deterministic polarization – the M1 marker iNOS showed no change in RAW/CPMV and a downregulation to 0.32 ± 0.16 fold in ID8/RAW/CPMV, while M2 marker Arg1 was upregulated in RAW/CPMV and showed no change in ID8/RAW/CPMV (Fig. S5A). The polarization of the macrophages in ID8/RAW/CPMV and ID8/RAW/sham was further characterized on the protein level by flow cytometry with a focus on the CPMV mediated macrophage activation [20,21]. However, we observed no significant change in all the M1-like or M2-like markers in the F4/80 labeled macrophages (Fig. S5B).

Activation of macrophage is strongly suggested by the TNF-α and phagocytosis results above. Therefore, we hypothesize that the macrophage activation mediated by CPMV accompanied by phagocytosis and TNF-α does not fall into the classical M1-M2 re-polarization axis. To further investigate the macrophage activation and phenotypic change, RNAseq was performed on the RAW cells isolated from ID8/RAW scaf-

folds. In this experiment, RAWs sorted from ID8/RAW/CPMV or ID8/RAW/sham are denoted as RAW/ID8/CPMV or RAW/ID8/sham, respectively.

Gene Set Enrichment Analysis (GSEA) revealed enrichment of both pro-inflammatory as well as pro-tumor genes upon CPMV treatment, including P53 pathway (M2 suppression [22]), coagulation (result of M1 polarization), wnt/ β-catenin signaling (pro-M2 [23,24], pro-OvCa [25]), glycolysis (pro-M1 [26,27]), KRAS signaling (pro-tumor associated macrophages, TAM [28]) both up and down (Fig. 4A), and TGF-β pathway (pro-M2) (Fig. 4A–C). Gene sets with controversial roles in macrophage polarization and cancer prognosis, namely Sialic acid (pro-M1 [29] but drives TAM [30]) and FOXO mediated transcription [31], were also enriched (Fig. 4C). In addition, the M1-marking NOS1 pathway was enriched in the sham group (Fig. 4D), confirming the qPCR data of iNOS downregulation in ID8/RAW/CPMV.

Despite the paradoxical results of gene set enrichment and M1/M2 marker expression (Fig. S5) toward a deterministic polarization toward classical M1 or M2 subtype, a notable activation and phenotypic change was definitively confirmed, which is also suggested by the clustering of the RAW/ID8/CPMV samples in principal component analysis (PCA) (Fig. 4E). On the other hand, MacSpectrum analysis suggested a low macrophage polarization index (MPI) and high activation-induced differentiation index (ADMI) in the RAW/ID8/sham, while 2 out of 3 RAW/ID8/CPMV samples showed a high MPI with low ADMI, and 1 out of 3 scored low in both MPI and ADMI (Fig. 4E, F, G). These results indicated that compared to each other, RAW/ID8/sham are more M2-like

macrophages, and RAW/ID8/CPMV are more transitional M1-like or pre-activation like macrophages [32], which suggested that the CPMV treatment reversed the pro-tumor immunity of the macrophages in the peritoneal OvCa spheroid model.

In addition, phagocytosis related enrichments were also observed, including phagocytic vesicle membrane, endoplasmic reticulum exit site (Fig. 4B), ER phagosome pathway and FOXO mediated transcription [31] (Fig. 4C). Pathways or biological components related to antigen presentation were also enriched due to CPMV treatment, including MHC protein complex, MHC-I peptide loading complex (Fig. 4B) and HDACs that deacetylate histones (Fig. 4C), in alignment with previous in vivo studies that macrophages were stimulated to regulate the downstream adaptive immune response to inhibit the development of ID8 inoculation induced ovarian cancer ([4,6,7]).

2.4. Macrophage-OvCa cell crosstalk

While CPMV induced enrichment of gene sets directly related to macrophage polarization and functionality, it was also notable that several gene set changes in TME were also altered due to CPMV, such as apical junction (Fig. 4A), GAP junction, apicolateral plasma membrane and connexin complex (Fig. 4B), VEGFR2 mediated vascular permeability (Fig. 4C), regulation of apoptotic process involved in development, response to platelet derived growth factor, and RAC1 pathway (Fig. 4D). Gene ontology enrichment was further applied to the significantly enriched gene sets shown in Fig. 4, which identified enhancement
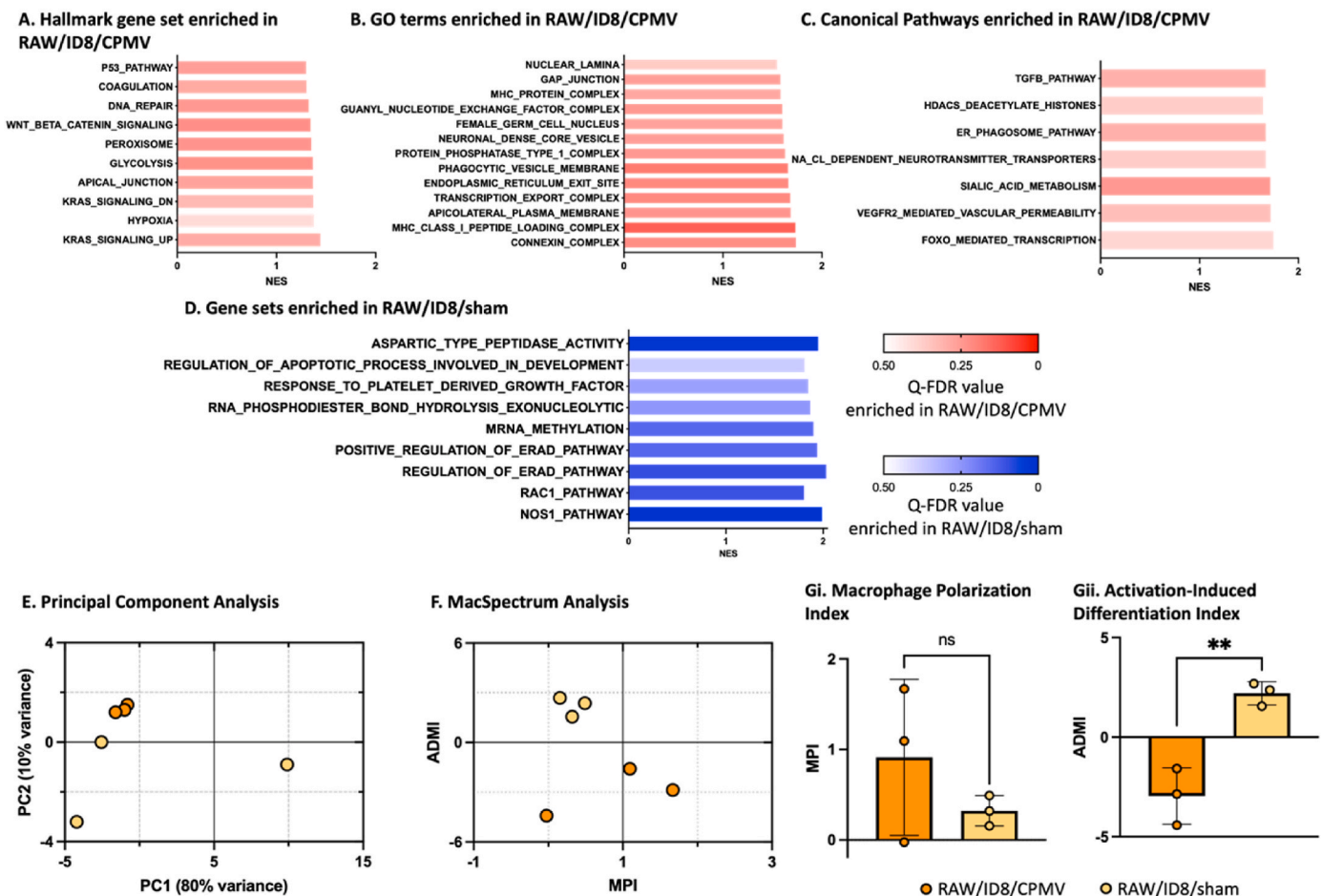

Fig. 4. RNA sequencing results of RAW264.7 isolated from ID8/RAW/CPMV or ID8/RAW/sham scaffolds revealing multifaceted macrophage activation. A-C. Gene sets enriched in RAW/ID8/CPMV D. Gene sets enriched in RAW/sham. (NES: normalized enrichment score, FDR: false discovery rate) E. Principal component analysis suggested clustering due to CPMV treatment. F. MacSpectrum analysis suggested that CPMV reversed the M2-like activation in the ID8/RAW spheroids. Statistics of the MPI (macrophage polarization index) and ADMI (activation-induced differentiation index) were summarized in Gi, Gii, respectively. (**P < 0.01).

in cell adhesion and cell junction potentially took place in the ID8/RAW spheroids when treated with CPMV.

GAP junctions are intercellular structures mediating cell adhesion and intercellular communication in epithelium tissue. Therefore, connexin43 (CXN43), the major protein to make the GAP junction complex was characterized in ID8/RAW scaffolds using immunofluorescence staining. As shown in Fig. 5B, while CXN43 was positive in most of the ID8/RAW/sham spheroids, the signal intensity was much stronger in ID8/RAW/CPMV spheroids, although mean fluorescence intensity did not show statistical significance (Fig. S6A). The sizes of the spheroids were also larger in the ID8/RAW/CPMV spheroids. The increase of CXN43 expression was more pronounced and statistically significant (P < 0.05*, Fig. S6B) in ID8/SUP spheroids. In the ID8/SUP/sham scaffolds, most of the spheroids were predominantly small, round, and CXN43-negative. In contrast, spheroids in the ID8/SUP/CPMV scaffold showed a more irregular shape and higher presence of CXN43 positive signal. These results suggested that RAW cells played a promoting role in the formation of GAP junction and cell-cell interaction in ID8/RAW

spheroids, which was further enhanced by the CPMV treatment. Since the enhancement was also observed in ID8/SUP scaffold where ID8s were only exposed to the RAW supernatants, the enhancement was conducted through paracrine secretion, potentially cytokine or exosome production, of the RAWs.

Expression of a panel of prognosis-related genes were further compared between ID8/RAW/CPMV vs. ID8/RAW/sham and ID8/SUP/CPMV vs. ID8/SUP/sham through qPCR (Fig. 5C), including epithelial-mesenchymal transition markers, E-cadherin, N-cadherin, and ZEB1, and tumorigenesis marker, MKi67, SMAD3, and CSF-1. In both ID8/RAW/CPMV and ID8/SUP/CPMV groups, E-cadherin mRNA expression was upregulated, indicating an enhanced epithelial phenotype and a corresponding reduction in the mesenchymal phenotype of the OvCa cells following CPMV treatment in the presence of macrophages. Additionally, a slight increase in N-cadherin was also observed in ID8/RAW/CPMV; however, it was downregulated in ID8/SUP/CPMV, along with a downregulation in ZEB1. This suggests that CPMV-triggered macrophage activation assisted the ID8 cells to manifest epithelial phenotype,
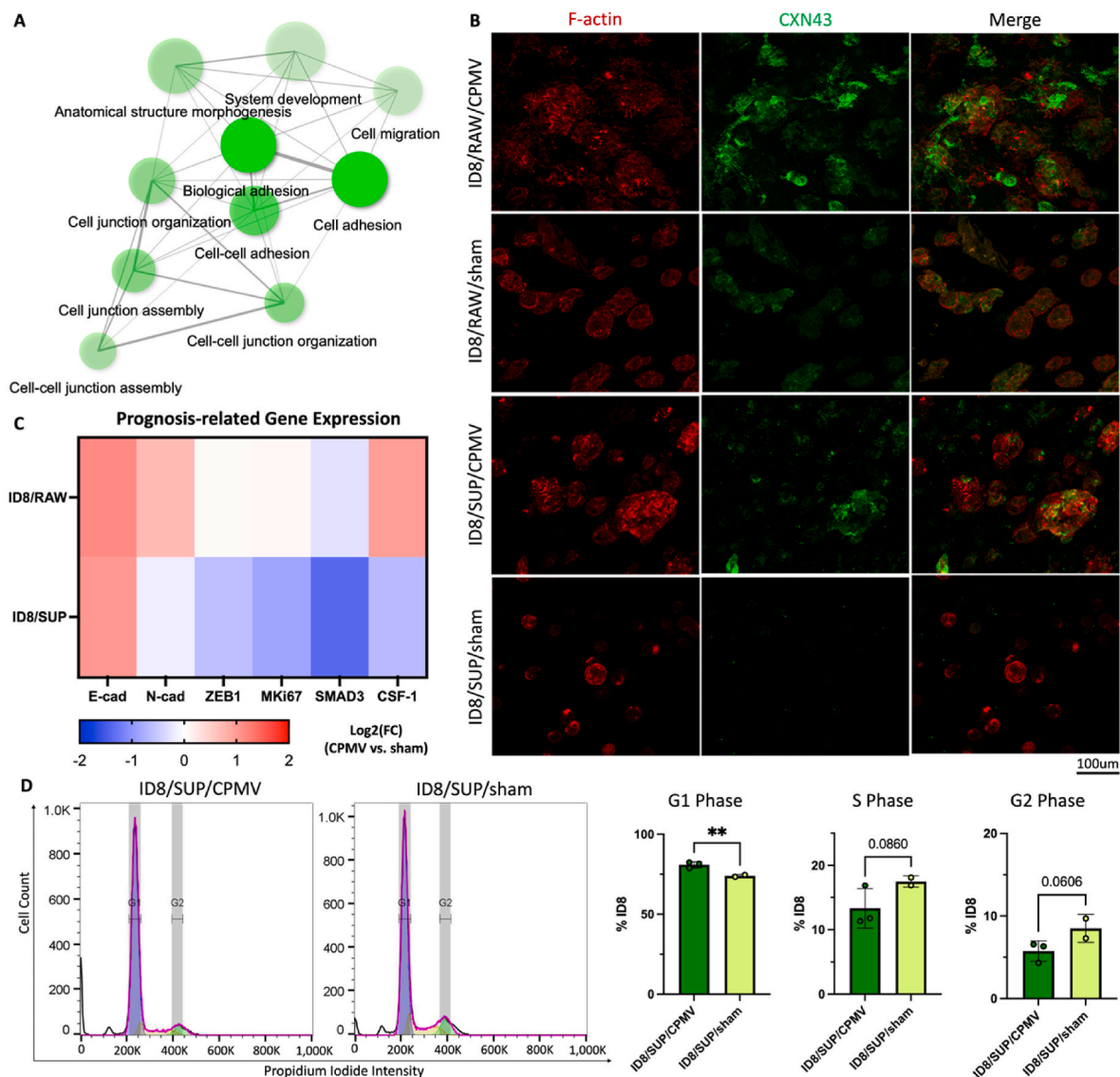

Fig. 5. CPMV stimulates macrophage to regulate OvCa cell organization. A. Gene ontology enrichment identified enhanced cell-cell adhesion and cell junction in RAW/ID8/CPMV. B. Gap junction protein, Connexin43 expression was upregulated by CPMV treatment in both ID8/RAW and ID8/SUP spheroids. C. Relative mRNA expression of epithelial-mesenchymal transition-related and tumorigenesis related genes in RAW/ID8 (RAW/ID8/CPMV vs. RAW/ID8/sham) and ID8/SUP (ID8/SUP/CPMV vs. ID8/SUP/sham) spheroids. D. Cell cycle analysis revealed increased G1 phase and reduced S and G2 phase cell percentage in ID8/SUP spheroids when treated with CPMV (**P < 0.01, ns: no significance).

which is related to a more favorable prognosis. MKi67, a proliferation marker, was not changed in ID8/RAW/CPMV, and downregulated in ID8/SUP/CPMV, while SMAD3 was downregulated in both scaffolds. CSF-1, a colony and spheroid promoter, interestingly, was upregulated in ID8/RAW/CPMV and downregulated in ID8/SUP/CPMV, suggesting that CPMV-activated RAW cells promoted spheroid growth in ID8/RAW spheroids, but their paracrine secreted products played an anti-tumor role.

ID8/SUP scaffolds were further characterized by the cell cycle. As shown in Fig. 5D, an increased G1 phase was observed in the ID8/SUP/CPMV scaffolds (P < 0.01**), along with a decrease in the percentage of S phase (P = 0.0860, ns) and G2 phase cells (P = 0.0606, ns).

3. Discussion

Aggressive ovarian cancer at advanced stages is characterized by intraperitoneal disseminated disease with formation of tumor spheroids and ascites. Spheroids are a major mediator of transcoelomic metastasis, their 3D architecture contributes to the development of chemo-resistance, and their cellular composition contributes to immune suppression and heterogeneity [2,8,33]. In vitro modeling of ovarian cancer spheroids requires a 3D architecture to support cell reorganization, appropriate matrix component to recapture the cell-ECM interaction, recapitulation of the cellular heterogeneity, compatibility with imaging and analysis, as well as reproducibility and scalability.

Our study showcased an advancement in the in vitro modeling of OvCa spheroids via DLP bioprinting to achieve rapid, high-throughput and highly consistent fabrication of the 3D architecture. Harnessing both the collagen-derived biochemical properties and the high reproducibility of photopolymerization, GelMA facilitated the adhesion, growth, and spontaneous spheroid formation of the OvCa cell. The choice of the material eliminates the batch-to-batch variation typically seen with collagen or Matrigel based hydrogel. Additionally, the rapid photo-initiated crosslinking precisely controlled by DLP printing ensured the consistency of size, stiffness, cell number and cell distribution in each scaffold. This high level of control surpasses traditional methods such as suspension culture [34], thermal gelation [35] or hanging drop [36]. Notably, the stiffness of the DLP-printed scaffolds can be precisely controlled by modulating the light intensity and exposure time [37]. In this study to model peritoneal spheroids, we employed a 10-s exposure using a 385 nm light source with an intensity of 15.28 mW/cm^2. This process yielded scaffolds with a stiffness of 148.7 ± 24.17Pa, comparable to that of ovarian cancer spheroids [38], and help to create an anti-inflammatory immune microenvironment conducive to the growth of cancer spheroids [39]. By extending the exposure time, we can fine-tune the stiffness to emulate other specific conditions, such as osmolarity-shocked OvCa spheroids (10–20 s exposure [38]) and ovarian tissue (35 s exposure [40]) (Fig. S1). By providing a consistent and controllable environment for cell growth and interaction, GelMA-based scaffolds offer a robust platform for studying complex biological processes and testing therapeutic interventions. This study highlights the practical advantages of GelMA in tissue engineering and its critical role in developing high-fidelity in vitro models for cancer research.

Here we developed an OvCa-Mac model as a novel system to study cancer immunotherapy – we used CPMV, a candidate for intratumoral immunotherapy, as the treatment test reagent. The 3D model was prepared using the murine ID8/Defb29/Vegf-A OvCa and RAW264.7 macrophage cell lines; this allowed initial modeling of cellular heterogeneity of OvCa spheroids. The murine ID8/Defb29/Vegf-A cells are a model of aggressive ovarian cancer [41] and the RAW264.7 cells are well-characterized with a consistent phenotype [42]. Although these cells are not human or primary cells, they provide good consistency as a platform for the exploration of CPMV mechanism while recapitulating the OvCa-macrophage co-organization [8], OvCa spheroid formation and increased migration potency [3] in the progression of the

carcinoma. As the first study to use DLP bioprinting to construct an in vitro OvCa model and the first to evaluate CPMV for OvCa in such a model, our primary aim was to demonstrate the capability and reproducibility of the 3D bioprinting strategy and validate the model for its suitability in evaluating the immunomodulatory agent for cancer immunotherapy [43]. Leveraging existing baseline data from animal and 2D cell culture studies using ID8 cells ensured consistency and reliability in our findings. The success in OvCa spheroid recapitulation also lays the foundation for more complex modeling with more physiologically relevant cells with the DLP bioprinting technology.

Recapitulation of multicellular OvCa spheroids in our model enables the investigation of CPMV as an intratumoral immunotherapy agent. Our study revealed inhibition of ID8 proliferation upon CPMV treatment, and this was mediated by the RAW cells within these spheroids. Such inhibition was previously recaptured by experiments in a traditional 2D culture setting [6], where, however, ID8 grow into a sheet, and ID8/RAW organization was not characterized. The previous study was focused on the immunogenicity in the consortium of the immune components, revealing the mechanism of inflammatory microenvironment and adaptive immune response by which CPMV shows tumor inhibition potency. Here, we dissect the variables in the immune system and specifically tackle the role of macrophage.

Phagocytosis is one of the major functions of macrophages which is often inhibited or dysregulated in the TME. These studies demonstrated that phagocytosis of OvCa cell was significantly enhanced in the spheroids upon CPMV therapy, with a notable population of RAW having engulfed both CPMV and ID8. Further, when the ID8 cells were not co-cultured with RAW cells, but treated with the RAW cells' supernatant, a significant reduction of the ID8 growth was also observed (Fig. 2B), demonstrating that alterations in the paracrine secretion of RAW also played a role, in addition to phagocytosis. Notably, TNF-α protein production of RAW cells was significantly induced by the treatment of CPMV. Also, while ID8 cells did not produce TNF-α regardless of CPMV treatment, ID8/RAW scaffolds produced more TNF-α than RAW-only scaffolds, which was further boosted by CPMV.

Stabilization of TNF mRNA upon TNF-α protein treatment is a feature of ovarian cancer cells [44]. In this study, it is one of the potential mechanisms through which the TNF mRNA content was elevated in the ID8 spheroids when treated by the supernatant of CPMV-primed RAWs (ID8/SUP/CPMV). Increased TNF mRNA was also observed, but not as pronounced, in the ID8 spheroids treated with TNF-α protein (ID8/tnf). These results highlight other mechanisms mediated by the macrophage paracrine secretion, which potentially include upregulated transcription and suppressed degradation, and are calling for further investigation. The change in the paracrine network of RAWs upon CPMV treatment was also suggested by distinct TNF pathway activation mode.

The apoptotic pathway activated by TNF-α appears to play a role in the observed effects of CPMV treatment on ID/RAW/CPMV. TNF-α induced apoptosis is activated through CASP8, leading to cell apoptosis mediated by CASP3. While CASP8 can also activate the MAPK pathway, which mediates inflammation and cell survival, our results showed distinct difference between the groups treated with CPMV and those treated with exogenous TNF-α protein.

In both the ID8/RAW/CPMV and ID8/SUP/CPMV groups, when TNF-α was produced by macrophages following CPMV treatment, there was notable increased CASP3 via CASP8, indicating strong activation of the apoptotic pathway. Interestingly, MAPK activation was negligible in these groups, suggesting that CPMV-induced TNF-α production primarily promoted apoptosis rather than cell survival pathways.

Conversely, in the ID8/tnf group treated with exogenous recombinant TNF-α protein, there was a notable elevation in CASP8 levels. This increase was accompanied by upregulations in MAPK and TRAF2, pathways associated with inflammation and cell survival. This differential activation suggested that while exogenous TNF-α protein can trigger apoptosis, it also activates survival pathways, potentially reducing its overall efficacy in inducing cell death.

These findings highlight the ability of CPMV to stimulate macrophages to a pro-inflammatory state, leading to enhanced TNF-α production. The increased TNF-α production in the ID8/RAW/CPMV group and its consequent induction of CASP3-mediated apoptosis, with minimal MAPK pathway activation, underscore the therapeutic potential of CPMV. By promoting a pro-inflammatory activation of macrophages and enhancing TNF-α production, CPMV may offer a more effective approach for inducing tumor cell death compared to direct TNF-α protein treatment.

In future studies, the role of TNF-α protein in the RAW supernatant can be dissected by TNF-α antibody neutralization, and the paracrine secretion can be further investigated by cytokine profiling and miRNA sequencing.

RNAseq was performed on the RAW cells sorted from ID8/RAW/CPMV and ID8/RAW/sham scaffolds, respectively, to further investigate the macrophage activation. Our sequencing data conveyed three major messages: 1) macrophage activation featured an inflammatory response and upregulated phagocytosis, 2) macrophage activation to reprogram adaptive immune response toward anti-tumor, which could be validated in a more complex model, 3) enhancements in cell-cell interactions and organization of cell junctions. The first two messages corroborate the previous animal studies [6,7] and upregulated phagocytosis and TNF-α production demonstrated in 2.2, suggest that, in OvCa-macrophage spheroids, CPMV reprogramed macrophages to inhibit OvCa cells growth. The activation of macrophages in the bioprinted OvCa spheroid model could not be classified into any subtype along the M1/M2 polarization axis. Nevertheless, Macspectrum analysis suggested CPMV treatment induced the trend to reverse the M2-like activation of macrophages in the macrophage-OvCa spheroid toward a transitional M1-like or pre-activation like state. The poorly characterized heterogeneity of macrophage activation has been increasingly recognized, especially in the context of tumor immune microenvironment [45–47]. Unfortunately, based on the available knowledge and methods, we have not been able to identify a specific subtype induced by CPMV treatment from the RNAseq data.

The third message conveyed by our RNAseq data was particularly intriguing – it is well-established that cell-cell interaction plays a pivotal role in modulating cell proliferation. Malignancies exhibit dysregulated proliferation, i.e., loss of growth restraint by contact inhibition [48]. It was also established that macrophage-epithelium crosstalk is essential in the maintenance of normal epithelium function [49,50]. Since upregulation of GAP junction related gene set was identified by the RNAseq data, while loss of GAP junction is a critical event in tumor progression [51,52], we investigated the expression of a major GAP junction protein, connexin43, in the ID8/RAW and ID8/SUP scaffolds and observed a notably stronger signal of the protein. Changes in the morphology of the spheroids were also observed. This data suggested that the CPMV also stimulates macrophage-mediated restoration of GAP junctions of the tumor cells that normalize growth control of these cells. This change also corroborated the qPCR data on several prognosis-related biomarkers, showing the retaining of epithelial phenotype and reversion of EMT [53]. Reduced proliferation and spheroid formation was also evident on ID8/SUP scaffolds, suggesting an essential anti-malignancy role played by the paracrine secretion of macrophage, although the pro-tumor differentiation when co-cultured with the OvCa cells were not completely reversed. The reduced cancer cell growth was also demonstrated by the cell cycle analysis on the ID8/SUP scaffolds, where we observed a significant G1 increase (Fig. 5D). G1 arrest is an essential result of restoring GAP junctions among cancer cells [54] and also a feature recaptured by OvCa cell treated with supernatant of M0 macrophages compared to M2 macrophages [55]. Further analysis on the supernatant components, i.e., cytokine network, growth factors, and miRNA components, will substantially contribute to elucidate the CPMV's macrophage activation patterns in the OvCa spheroids. These results also suggest that CPMV is a strong candidate for the regulation of macrophage-epithelium crosstalk, offering the potential for broader application, such as treatment for lung

[50], gut [56], and pancreatic diseases [49,57].

In summary, we have successfully developed an initial version of a clinically relevant in vitro OvCa spheroid model using DLP-based 3D bioprinting. Developing in vitro models for evaluating immunotherapy is a critical but challenging need due to the complexity of the immune systems. Our study addresses this need by leveraging DLP bioprinting for constructing an in vitro OvCa model, and its usage is demonstrated by studying CPMV as an immunotherapeutic agent. Our model enabled in-depth investigation of CPMV mediated cancer immunotherapy on the OvCa spheroids, elucidating the immune-activation via macrophages, and revealed a new mechanism to restore the cell-cell junction. The versatile platform is translatable to a wide variety of cell sources, i.e., mouse primary cells, patient biopsies, and iPSC differentiated cells. The use of GelMA is an innovative approach to utilize biomaterial for creating high-fidelity, immune-compatible tumor models. These findings will provide a robust foundation for further studies and designs on CPMV adjuvant therapy to accelerate its bench-to-bedside translation.

4. Methods

4.1. Cell culture

ID8-Defb29 Vegf-Luc cells (denoted as ID8 for simplicity) were maintained and propagated in RPMI 1640 medium (Cat# 11875093, Gibco) supplemented with 1 mM sodium pyruvate (Cat# 11360070, Gibco), 1 mM 2-mercaptoethanol (Cat# 21985023, Gibco), 10 % (v/v) fetal bovine serum (FBS, Cat# SH30396.03HI, Cytiva) and 1$\times$ Penicillin-Streptomycin (Cat# P4333, Sigma-Aldrich). This combination is referred to as ID8 medium for simplicity in this study. The cells are passaged every 2 days by disassociating with 0.25 % Trypsin-EDTA (Cat# 25200056, Gibco), pelleting and seeding 1:3 to new flasks. RAW264.7 cells (TBI-71) were purchased from ATCC. The cells were maintained and propagated in complete medium comprised of Dulbecco's Modified Eagle Medium (Cat# 11965092, Gibco) and 10 % (v/v) FBS. The cells are passaged every 2 days, for which the cells were disassociated by gentle rinsing with Dulbecco's phosphate-buffered saline (DPBS, Cat# 14190144, Gibco), pelleting and seeding 1:3 to new flasks. Both cells were incubated at 37 $^{\circ}C$ under 5 % CO_2.

4.2. CPMV & CPMV-Cy5 preparation

CPMV was propagated in black eyed pea No. 5 plants and purified as described previously [18,58]. CPMV-Cy5 was synthesized via *N-Hydroxysuccinimide* (NHS) chemistry using the previously published protocol [18,19] Simply, 1500-M excess of sulfo-Cy5 NHS ester (777.95 g/mol, Lumiprobe) was mixed with 2 mg/mL CPMV (final concentration, molecular weight = 5.6 $\times$ 10^6 g/mol) in 1$\times$ PBS to react with the CPMV's surface exposed lysine residues; the reaction was carried out at room temperature for 2 h. To remove unconjugated Cy5 molecules, the reaction mixture was loaded on the Amicon Ultra-0.5 mL centrifugal filters with a 100-kDa cutoff (Millipore Sigma) and washed 4 times with 1$\times$ PBS. Purified CPMV-Cy5 was stored at 4 $^{\circ}$C. The concentrations of CPMV and CPMV-Cy5 were determined by UV–Vis spectrophotometry using a NanoDrop 2000 spectrophotometer (ThermoFisher Scientific) with the extinction coefficient (ε) of CPMV at 260 nm = 8.1 mL/(mg x cm). The number of conjugated Cy5 per CPMV-Cy5 was calculated using the molar extinction coefficient (ε) for sulfo-Cy5 (271,000 L/(mol x cm)) at 647 nm.

4.3. CPMV and CPMV-Cy5 characterization

Agarose gel electrophoresis – 20 µg CPMV or CPMV-Cy5 were mixed with 6$\times$ Gel Loading Purple dye (Biolabs) and loaded onto a 1 % (w/v) agarose gel that was prepared with 1 $\times$ Tris acetate EDTA (TAE) buffer and 1$\times$ GelRed nucleic acid gel stain (Gold Biotechnologies). The gel was run at 100 V and 300 mA for 35 min in 1$\times$ TAE buffer. RAN (UV)

and Cy5 (Multi-Color Red Filter) images were first captured using a ProteinSimple FluorChem R imager. Gel was then stained with Coomassie Brilliant Blue for protein imaging.

SDS-PAGE – CPMV and CPMV-Cy5 were mixed with $4 \times$ lithium dodecylsulfate buffer (Thermo Fisher Scientific) and $10 \times$ reducing agent (Invitrogen) and heated at 95 °C for 8 min for sample preparation. 10 μg denatured CPMV and CPMV-Cy5 were then loaded onto a 4–12 % NuPAGE gel (Thermo Fisher Scientific) and run at 200 V, 120 mA, and 25 W for 35 min in $1\times$ MOPS buffer (Thermo Fisher Scientific). Cy5 image was captured prior to Coomassie Brilliant Blue staining for protein detection. Images were captured using a ProteinSimple FluorChem R imager.

Dynamic light scattering (DLS) – 100 μL of 1 mg/mL CPMV and CPMV-Cy5 were loaded into a cuvette and then analyzed using a Zetasizer Nano ZSP/Zen5600 instrument (Malvern Panalytical). Each sample was measured 3 times at room temperature.

Transmission electron microscopy (TEM) – 4 μL of 0.5 mg/mL CPMV and CPMV-Cy5 were applied to a glow-discharged carbon film with a 300-mesh Cu grid for 30 s, then blotted using filter paper; grids were then washed once using 4 μL Mili-Q water, blotted; lastly, 4 μL 1 % (w/v) uranyl acetate (Electron Microscopy Sciences) was applied onto each grid for 30 s, then blotted and airdried for imaging. Grids were imagined using a Talos TEM (Thermo Fisher Scientific) at a nominal magnification of $120,000 \times$.

The characterization results are shown in Fig. S3.

4.4. Bioink composition

A bioink comprised of 5 % (w/v) gelatin methacrylate (GelMA), 0.6 % (w/v) lithium phenyl-2,4,6-trimethylbenzoylphosphinate (LAP, Cat# 900,889, Sigma-Aldrich) in DPBS was used throughout the study. GelMA was synthesized in house in a 0.25 M carbonate-biocarbonate (CB) buffer, where 10 % (w/v) type A gelatin (Cat# G2500, Sigma-Aldrich) was subjected to a reaction with methacrylic anhydride (MA, Cat# 276,685, Sigma-Aldrich) at MA/gelatin ratio of 0.085 mL/g for 1 h at 50 °C [59]. The GelMA was purified by dialysis in 12–14 kDa cutoff tubings (Cat. # 132,706, Spectrum Labs) in MilliQ water for 3 days at 37 °C, lyophilized, and dissolved in DPBS to prepare a 20 % (w/v) stock solution. GelMA and LAP were mixed well by pipetting immediately prior to mixing with cells.

For conditions illustrated in Fig. 2Ai, ID8 and RAW264.7 cells were collected by the same disassociation procedure as described above, counted with a hemacytometer, and combined in a 1:1 ratio. Immediately prior to printing, the cells are pelleted by centrifuge at 300 g for 5 min and mixed with the bioink at a cell density of 5 M/mL of each (10 M/mL total). For conditions illustrated in Fig. 2Aii, only 5 M/mL of ID8 or RAW264.7 were mixed with the bioink for printing.

For scaffolds shown in Fig. 1B and E, ID8 cells were stained with CellTracker Green (Cat# C7025, Invitrogen), and RAW264.7 cells were stained with CellTracker Orange (Cat# C34551, Invitrogen) prior to printing, respectively. The CellTracker dyes were dissolved in dimethylsulfoxide (DMSO, Cat# D12345, Invitrogen) to prepare a 10 mM stock solution, and diluted in serum-free DMEM to 10 μM, which is used to incubate with the cells.

For scaffolds used in the flow cytometry-based phagocytosis assay, ID8 cells were stained with CellTracker Green prior to printing, while RAW264.7 cells were not stained.

4.5. Bioprinting and treatment

Bioprinting was performed on an in-house built DLP-based bioprinter with a 385 nm LED light source. Glass slides and polydimethylsiloxane (PDMS) sheets were used to assemble the bioink reservoir, and methacrylate coverslips, prepared per a previously established protocol [15,60], were used as the substrate for printing. Light power at 15.28 mW/cm^2, 10 s exposure for a 250 μm thickness was

applied throughout this study. A 3 mm × 3 mm square-shape mask was used for all the scaffolds unless otherwise specified.

The scaffolds were incubated in 24 well plates with 500 μL ID8 medium for each, regardless of cell composition. After 48 h, the medium was replaced with 500 μL ID8 medium with 20 μg/mL CPMV for CPMV treated groups (ID8/RAW/CPMV, ID8/CPMV, RAW/CPMV), or 500 μL fresh ID8 medium for sham groups (ID8/RAW/sham, ID8/sham, RAW/sham). The samples are subjected to analysis after 24 h of CPMV treatment. For ID8/SUP/CPMV or ID8/SUP/sham, after 48 h of incubation, the medium was replaced with the supernatant of RAW/CPMV or RAW/sham which has been treated with CPMV for 24 h, and the samples were treated with the supernatant for 24 h prior to analysis. For ID8/tnf, ID8 scaffolds were treated with ID8 medium containing 150 ng/mL recombinant mouse TNF alpha protein (Cat# ab259411, Abcam) for 24 h after 48 h of incubation.

4.6. Cell viability assay

The viability of ID8 cells for the evaluation of growth profile and CPMV inhibition was investigated by luciferase assay and marked by the bioluminenscence. At the time point for analysis, the cells were washed with DPBS and collected by $1\times$ cell lysis buffer (Cat# E1531, Promega). The samples were vortexed for 15 s to ensure a full lysis, and supernatant was collected after centrifuging at 12,000 g for 30 s. The samples were kept on ice until analysis to ensure protein integrity. The luciferase assay reagent (LAR, Cat# E1501, Promega) was prepared as instructed by the manufacturer. 20 μL sample and 100 μL LAR was directly mixed in a white, flat-bottom 96 well plate (Cat# IP-DP35F-96-W, Stellar Scientific) by pipetting, and assayed immediately for bioluminescence by a Tecan Infinite 200 Pro plate reader, with an integration time of 1000 ms.

4.7. Staining and imaging

Brightfield images and the fluorescent image in Fig. 1B–D were taken on a Leica DMI 6000 B fluorescent microscope. The CellTracker Green/Orange labeled spheroids was imaged by a Leica SP8 lighting confocal microscope with a Z axis scan and reconstruction. The samples were fixed with 4 % paraformaldehyde (PFA, Cat# J19943. K2, Thermo Scientific Chemicals) for 15 min and kept in DPBS. The spheroid count and size were quantified with ImageJ with the 'measure' and 'analyze particles' function.

Immunofluorescent staining was performed after the samples have been fixed with 4 % PFA for 15 min. The samples were then permeabilized with 0.1 % (v/v) triton-x-100 (Cat# ×100, Sigma-Aldrich) for 10 min and blocked with 2 % bovine serum albumin (BSA, Cat# A9418, Sigma-Aldrich) for 30 min at room temperature. F-actin was labeled by Phalloidin eFluor 660 (Cat# 50-6559-05, Invitrogen) at its working concentration as instructed by the manufacturer for 20 min at room temperature. Nuclei was labeled by 4',6-Diamidino-2-Phenylindole (DAPI, D3571, Invitrogen) at 1 μg/mL for 20 min at room temperature. For connexin43 (CXN43) imaging, the samples were incubated with primary Connexin43 Rabbit mAb (Cat# 83,649, Cell Signaling Technology) at 1:200 in 4 °C overnight. After washing, the samples were incubated in a CF543-conjugated donkey anti-rabbit secondary antibody (Cat# E20308, Biotium) at 1 : 200 at room temperature for 1 h, followed by F-actin labeling. All the staining was performed with cell staining buffer (Cat# 420,201, BioLegend). Samples were mounted on glass slides with ProLong Gold Antifade Mountant (Cat# P36930, Invitrogen) for optimized imaging quality. Images were taken on the Leica SP8. All the connexin43 images were taken under the same laser settings to compare their signal intensities. The mean fluorescence intensity of connexin43 were analyzed and quantified using an in-house developed ImageJ-based program by masking with the F-actin signal.

4.8. Real time quantitative polymerase chain reaction (qPCR)

RNA was extracted by a Trizol-based method using a spin column-based kit (Direct-zol RNA Microprep Kits, Cat# R2062, Zymo Research). Purity and concentration of RNA was examined by measurement of absorbance at 260/280 nm, followed conversion to cDNA with ProtoScript First Strand cDNA Synthesis Kit (Cat# E6300, New England BioLabs) per the manufacturer's instructions. qPCR was conducted with Luna Universal qPCR Master Mix (Cat# M3003, New England BioLabs) on a Quantstudio 3 system (ThermoFisher). Primer sequences are provided in Table S2. Data was processed by $2^{-\Delta\Delta Ct}$ method normalized to GAPDH. Fold change was compared between CPMV treated and sham of same scaffold conditions.

4.9. Flow cytometry

Cells were disassociated from the bioprinted scaffolds by digestion with 0.25 % Trypsin-EDTA for 8 min at 37 °C, followed by washing with ice cold DPBS twice.

4.10. Phagocytosis assay

Cells were incubated with PE/Cyanine5 anti-mouse F4/80 antibody (Cat# 123,111, BioLegend) at 1:200 for 1 h at 4 °C, followed by fixation with stabilizing fixative (Cat# 338,036, BD Bioscience). Cells were then resuspended in a FACS buffer containing 1 % (w/v) BSA, 0.1 % (w/v) sodium azide in DPBS and analyzed with BD Accuri C6 flow cytometer.

4.11. Cell cycle analysis

Cells were fixed and permeabilized with 70 % Ethanol at 4 °C for 2 h and stained with 50 μg/mL Propidium Iodide (Cat# P3566, Invitrogen) supplemented with 100 μg/mL RNAse A (Cat# 7013, Cell Signaling Technology). Cells were then resuspended in a FACS buffer containing 1 % (w/v) BSA, 0.1 % (w/v) sodium azide in DPBS and analyzed with BD Accuri C6 flow cytometer.

4.12. Polarization analysis

Cells were first stained with LIVE/DEAD Fixable Aqua Dead Cell Stain Kit (Thermo Fisher Scientific) on ice for 15 min. After washing, cells were blocked with anti-CD16/32 Fc block (Biolegend) on ice for 15 min. Cells were then washed and stained with Pacific Blue anti-CD45 antibody (Biolegend), Brilliant Violet 785 anti-F4/80 antibody (Biolegend), PE anti-CD80 antibody (Biolegend), Brilliant Violet 605 anti-CD86 antibody (Biolegend), APC MHC-II antibody (Thermo Fisher Scientific), and PerCP-Cy5.5 anti-CD206 antibody (Biolegend) on ice for 30 min. All cells were then washed, fixed, and permeabilized using the BD Cytofix/Cytoperm Plus Kit (BD). Lastly, cells were stained with PE/Cy7 anti-iNOS antibody and Alexa Fluor 488 anti-Arginase 1 antibody (Thermo Fisher Scientific) for 30 min. Cells were washed and resuspended in FACS buffer and analyzed using a BD FACSCelesta flow cytometer. UltraComp eBeads (Thermo Fisher Scientific) were used to prepare single color staining for compensation.

All the flow cytometry data was processed using Flowjo_v10.7 software.

4.13. ELISA

Production of TNF-α protein was evaluated by ELISA using a Mouse TNF-alpha Quantikine ELISA Kit (Cat# MTA00B, R&D systems) per the manufacturer's protocol. The supernatant of each scaffold was assayed directly after collection.

4.14. Bulk RNA sequencing (RNAseq)

RAW cells were isolated from ID8/RAW/CPMV or ID8/RAW/sham scaffolds for RNAseq. The scaffolds were digested with 0.25 % Trypsin-EDTA for 8 min at 37 °C to release the cells, and RAW cells were selectively collected via magnetic-activated cell sorting using Anti-F4/80 magnetic microbeads (Cat# 130-110-443, Miltenyi Biotec) and MS Separation columns (Cat# 130-042-201, Miltenyi Biotec). RNA was prepared using the same procedure as qPCR. The RNA quality evaluation and sequencing were performed by Novogen Inc. using their eukaryotic RNA-Seq cDNA library pipeline. The data quality was evaluated by FastQC, followed by trimming via Trimmomatic, aligned with HISAT2, and annotated with StringTie. Differential gene expression was analyzed by DESeq2. Gene Set Enrichment Analysis was performed by GSEA_4.3.2 (Broad Institute). Gene ontology enrichment analysis was conducted with ShinyGO 0.75.

4.15. Statistical analysis

Data are presented as mean $\pm$ standard deviation unless otherwise specified. All experiments were performed with at least 3 biological replications. Pairwise comparison was performed with Student's *t*-test. *P* values < 0.05 were considered significant.

CRediT authorship contribution statement

Yi Xiang: Writing – review & editing, Writing – original draft, Visualization, Validation, Project administration, Methodology, Investigation, Formal analysis, Data curation, Conceptualization. **Zhongchao Zhao:** Writing – review & editing, Writing – original draft, Visualization, Validation, Methodology, Investigation, Formal analysis, Data curation, Conceptualization. **Emmie J. Yao:** Writing – review & editing, Investigation. **Alis Balayan:** Writing – review & editing, Software, Formal analysis. **Steven N. Fiering:** Writing – review & editing, Writing – original draft, Funding acquisition, Formal analysis, Conceptualization. **Nicole F. Steinmetz:** Writing – review & editing, Funding acquisition, Formal analysis, Conceptualization. **Shaochen Chen:** Writing – review & editing, Supervision, Funding acquisition, Formal analysis, Conceptualization.

Declaration of competing interest

Nicole F. Steinmetz reports a relationship with Mosaic ImmunoEnginering Inc. that includes: equity or stocks. Steven N. Fiering reports a relationship with Mosaic ImmunoEnginering Inc. that includes: equity or stocks. Nicole F. Steinmetz reports a relationship with Pokometz Scientific LLC that includes: consulting or advisory. If there are other authors, they declare that they have no known competing financial interests or personal relationships that could have appeared to influence the work reported in this paper.

Data availability

Data will be made available on request.

UCSD, a member of the National Nanotechnology Coordinated Infrastructure (NNCI), which is supported by the National Science Foundation (Grant ECCS-2025752).

Appendix A. Supplementary data

Supplementary data to this article can be found online at https://doi.org/10.1016/j.biomaterials.2024.122663.

References

[1] R.J. Kathawala, A. Kudelka, B. Rigas, The chemoprevention of ovarian cancer: the need and the options, Curr Pharmacol Rep 4 (2018) 250–260, https://doi.org/10.1007/s40495-018-0133-6.

[2] K. Shield, M.L. Ackland, N. Ahmed, G.E. Rice, Multicellular spheroids in ovarian cancer metastases: biology and pathology, Gynecol. Oncol. 113 (2009) 143–148, https://doi.org/10.1016/j.ygyno.2008.11.032.

[3] L. Long, Y. Hu, T. Long, X. Lu, Y. Tuo, Y. Li, et al., Tumor-associated macrophages induced spheroid formation by CCL18-ZEB1-M-CSF feedback loop to promote transcoelomic metastasis of ovarian cancer, J Immunother Cancer 9 (2021), https://doi.org/10.1136/jitc-2021-003973.

[4] P.H. Lizotte, A.M. Wen, M.R. Sheen, J. Fields, P. Rojanasopondist, N.F. Steinmetz, et al., In situ vaccination with cowpea mosaic virus nanoparticles suppresses metastatic cancer, Nat. Nanotechnol. 11 (2016) 295–303, https://doi.org/10.1038/nnano.2015.292.

[5] D. Alonso-Miguel, G. Valdivia, D. Guerrera, M.D. Perez-Alenza, S. Pantelyushin, A. Alonso-Diez, et al., Neoadjuvant in situ vaccination with cowpea mosaic virus as a novel therapy against canine inflammatory mammary cancer, J Immunother Cancer 10 (2022), https://doi.org/10.1136/jitc-2021-004044.

[6] C. Wang, S.N. Fiering, N.F. Steinmetz, Cowpea mosaic virus promotes anti-tumor activity and immune memory in a mouse ovarian tumor model, Adv. Ther. 2 (2019), https://doi.org/10.1002/adtp.201900003.

[7] C. Wang, N.F. Steinmetz, CD47 blockade and cowpea mosaic virus nanoparticle in situ vaccination triggers phagocytosis and tumor killing, Adv. Healthcare Mater. 8 (2019), https://doi.org/10.1002/adhm.201801288.

[8] M. Yin, X. Li, S. Tan, H.J. Zhou, W. Ji, S. Bellone, et al., Tumor-associated macrophages drive spheroid formation during early transcoelomic metastasis of ovarian cancer, J. Clin. Invest. 126 (2016) 4157–4173, https://doi.org/10.1172/JCI87252.

[9] C. Mao, V. Beiss, G.W. Ho, J. Fields, N.F. Steinmetz, S. Fiering, In situ vaccination with cowpea mosaic virus elicits systemic antitumor immunity and potentiates immune checkpoint blockade, J Immunother Cancer 10 (2022), https://doi.org/10.1136/jitc-2022-005834.

[10] C. Nero, G. Vizzielli, D. Lorusso, E. Cesari, G. Daniele, M. Loverro, et al., Patient-derived organoids and high grade serous ovarian cancer: from disease modeling to personalized medicine, J. Exp. Clin. Cancer Res. 40 (2021), https://doi.org/10.1186/s13046-021-01917-7.

[11] E.A. White, H.A. Kenny, E. Lengyel, Three-dimensional modeling of ovarian cancer, Adv. Drug Deliv. Rev. 79 (2014) 184–192, https://doi.org/10.1016/j.addr.2014.07.003.

[12] S. Zhang, S. Iyer, H. Ran, I. Dolgalev, S. Gu, W. Wei, et al., Genetically defined, syngeneic organoid platform for developing combination therapies for ovarian cancer, Cancer Discov. 11 (2021) 362–383, https://doi.org/10.1158/2159-8290.CD-20-0455.

[13] O. Kopper, C.J. de Witte, K. Lõhmussaar, J.E. Valle-Inclan, N. Hami, L. Kester, et al., An organoid platform for ovarian cancer captures intra- and interpatient heterogeneity, Nat. Med. 25 (2019) 838–849, https://doi.org/10.1038/s41591-019-0422-6.

[14] M. Tang, J.N. Rich, S. Chen, Biomaterials and 3D bioprinting strategies to model glioblastoma and the blood–brain barrier, Adv. Mater. 33 (2021), https://doi.org/10.1002/adma.202004776.

[15] M. Tang, S.K. Tiwari, K. Agrawal, M. Tan, J. Dang, T. Tam, et al., Rapid 3D bioprinting of glioblastoma model mimicking native biophysical heterogeneity, Small 17 (2021), https://doi.org/10.1002/smll.202006050.

[16] M.S. Haney, C.J. Bohlen, D.W. Morgens, J.A. Ousey, A.A. Barkal, C.K. Tsui, et al., Identification of phagocytosis regulators using magnetic genome-wide CRISPR screens, Nat. Genet. 50 (2018) 1716–1727, https://doi.org/10.1038/s41588-018-0254-1.

[17] G.H. Nam, Y. Hong, Y. Choi, G.B. Kim, Y.K. Kim, Y. Yang, et al., An optimized protocol to determine the engulfment of cancer cells by phagocytes using flow cytometry and fluorescence microscopy, J. Immunol. Methods 470 (2019) 27–32, https://doi.org/10.1016/j.jim.2019.04.007.

[18] Z. Zhao, O.A. Ortega-Rivera, Y.H. Chung, A. Simms, N.F. Steinmetz, A co-formulated vaccine of irradiated cancer cells and cowpea mosaic virus improves ovarian cancer rejection, J. Mater. Chem. B 11 (2023) 5429–5441, https://doi.org/10.1039/d2tb02355e.

[19] Y.H. Chung, H. Cai, N.F. Steinmetz, Viral nanoparticles for drug delivery, imaging, immunotherapy, and theranostic applications, Adv. Drug Deliv. Rev. 156 (2020) 214–235, https://doi.org/10.1016/j.addr.2020.06.024.

[20] A. Agrawal, M. Manchester, Differential uptake of chemically modified cowpea mosaic virus nanoparticles in macrophage subpopulations present in inflammatory and tumor microenvironments, Biomacromolecules 13 (2012) 3320–3326, https://doi.org/10.1021/bm3010885.

[21] L. Liu, J.V. Stokes, W. Tan, S.B. Pruett, An optimized flow cytometry panel for classifying macrophage polarization, J. Immunol. Methods 511 (2022), https://doi.org/10.1016/j.jim.2022.113378.

[22] L. Li, D.S.W. Ng, W.C. Mah, F.F. Almeida, S.A. Rahmat, V.K. Rao, et al., A unique role for p53 in the regulation of M2 macrophage polarization, Cell Death Differ. 22 (2015) 1081–1093, https://doi.org/10.1038/cdd.2014.212.

[23] J. Yang, Y. Wang, D. Yang, J. Ma, S. Wu, Q. Cai, et al., Wnt/β-catenin signaling regulates lipopolysaccharide-altered polarizations of RAW264.7 cells and alveolar macrophages in mouse lungs, Eur. J. Inflamm. 19 (2021), https://doi.org/10.1177/20587392211059362.

[24] Y. Yang, Y.C. Ye, Y. Chen, J.L. Zhao, C.C. Gao, H. Han, et al., Crosstalk between hepatic tumor cells and macrophages via Wnt/β-catenin signaling promotes M2-like macrophage polarization and reinforces tumor malignant behaviors, Cell Death Dis. 9 (2018), https://doi.org/10.1038/s41419-018-0818-0.

[25] V.H.L. Nguyen, R. Hough, S. Bernaudo, C. Peng, Wnt/β-catenin signalling in ovarian cancer: insights into its hyperactivation and function in tumorigenesis, J. Ovarian Res. 12 (2019), https://doi.org/10.1186/s13048-019-0596-z.

[26] Y. Liu, R. Xu, H. Gu, E. Zhang, J. Qu, W. Cao, et al., Metabolic reprogramming in macrophage responses, Biomark. Res. 9 (2021), https://doi.org/10.1186/s40364-020-00251-y.

[27] A. Viola, F. Munari, R. Sánchez-Rodríguez, T. Scolaro, A. Castegna, The metabolic signature of macrophage responses, Front. Immunol. 10 (2019), https://doi.org/10.3389/fimmu.2019.01462.

[28] H. Liu, Z. Liang, C. Zhou, Z. Zeng, F. Wang, T. Hu, et al., Mutant KRAS triggers functional reprogramming of tumor-associated macrophages in colorectal cancer, Signal Transduct. Targeted Ther. 6 (2021), https://doi.org/10.1038/s41392-021-00534-2.

[29] X. Hu, Y. Li, Q. Chen, T. wang, L. Ma, W. Zhang, et al., Sialic acids promote macrophage M1 polarization and atherosclerosis by upregulating ROS and autophagy blockage, Int. Immunopharm. 120 (2023), https://doi.org/10.1016/j.intimp.2023.110410.

[30] E. Rodriguez, K. Boelaars, K. Brown, R.J. Eveline Li, L. Kruijssen, S.C.M. Bruijns, et al., Sialic acids in pancreatic cancer cells drive tumour-associated macrophage differentiation via the Siglec receptors Siglec-7 and Siglec-9, Nat. Commun. 12 (2021), https://doi.org/10.1038/s41467-021-21550-4.

[31] S.J. Rong, C.L. Yang, F.X. Wang, F. Sun, J.H. Luo, T.T. Yue, et al., The essential role of FoxO1 in the regulation of macrophage function, BioMed Res. Int. 2022 (2022), https://doi.org/10.1155/2022/1068962.

[32] C. Li, A. Menoret, C. Farragher, Z. Ouyang, C. Bonin, P. Holvoet, et al., Single-cell transcriptomics-based MacSpectrum reveals macrophage activation signatures in diseases, JCI Insight 4 (2019), https://doi.org/10.1172/jci.insight.126453.

[33] S. Al Habyan, C. Kalos, J. Szymborski, L. McCaffrey, Multicellular detachment generates metastatic spheroids during intra-abdominal dissemination in epithelial ovarian cancer, Oncogene 37 (2018) 5127–5135, https://doi.org/10.1038/s41388-018-0317-x.

[34] T. Velletri, C.E. Villa, D. Cilli, B. Barzaghi, P. Lo Riso, M. Lupia, et al., Single cell-derived spheroids capture the self-renewing subpopulations of metastatic ovarian cancer, Cell Death Differ. 29 (2022) 614–626, https://doi.org/10.1038/s41418-021-00878-w.

[35] M. Liu, X. Zhang, C. Long, H. Xu, X. Cheng, J. Chang, et al., Collagen-based three-dimensional culture microenvironment promotes epithelial to mesenchymal transition and drug resistance of human ovarian cancer: in vitro, RSC Adv. 8 (2018) 8910–8919, https://doi.org/10.1039/c7ra13742g.

[36] S. Raghavan, P. Mehta, Y. Xie, Y.L. Lei, G. Mehta, Ovarian cancer stem cells and macrophages reciprocally interact through the WNT pathway to promote pro-tumoral and malignant phenotypes in 3D engineered microenvironments, J Immunother Cancer 7 (2019), https://doi.org/10.1186/s40425-019-0666-1.

[37] C. Yu, J. Schimelman, P. Wang, K.L. Miller, X. Ma, S. You, et al., Photopolymerizable biomaterials and light-based 3D printing strategies for biomedical applications, Chem. Rev. (2020), https://doi.org/10.1021/acs.chemrev.9b00810 acs.chemrev.9b00810.

[38] C. Conrad, K.M. Gray, K.M. Stroka, I. Rizvi, G. Scarcelli, Mechanical characterization of 3D ovarian cancer nodules using brillouin confocal microscopy, Cell. Mol. Bioeng. 12 (2019) 215–226, https://doi.org/10.1007/s12195-019-00570-7.

[39] Z. Zhuang, Y. Zhang, S. Sun, Q. Li, K. Chen, C. An, et al., Control of matrix stiffness using methacrylate-gelatin hydrogels for a macrophage-mediated inflammatory response, ACS Biomater. Sci. Eng. 6 (2020) 3091–3102, https://doi.org/10.1021/acsbiomaterials.0c00295.

[40] T.I.R. Hopkins, V.L. Bemmer, S. Franks, C. Dunlop, K. Hardy, I.E. Dunlop, Micromechanical mapping of the intact ovary interior reveals contrasting mechanical roles for follicles and stroma, Biomaterials 277 (2021), https://doi.org/10.1016/j.biomaterials.2021.121099.

[41] C.F. Hung, Y.C. Tsai, L. He, T.C. Wu, Control of mesothelin-expressing ovarian cancer using adoptive transfer of mesothelin peptide-specific CD8+ T cells, Gene Ther. 14 (2007) 921–929, https://doi.org/10.1038/sj.gt.3302913.

[42] B. Taciak, M. Białasek, M. Braniewska, Z. Sas, P. Sawicka, Ł. Kiraga, et al., Evaluation of phenotypic and functional stability of RAW 264.7 cell line through serial passages, PLoS One 13 (2018), https://doi.org/10.1371/journal.pone.0198943.

[43] P.C. Searson, The Cancer Moonshot, the role of in vitro models, model accuracy, and the need for validation, Nat. Nanotechnol. 18 (2023) 1121–1123, https://doi.org/10.1038/s41565-023-01486-0.

[44] P.W. Szlosarek, M.J. Grimshaw, H. Kulbe, J.L. Wilson, G.D. Wilbanks, F. Burke, et al., Expression and regulation of tumor necrosis factor α in normal and malignant

ovarian epithelium, Mol. Cancer Therapeut. 5 (2006) 382–390, https://doi.org/10.1158/1535-7163.MCT-05-0303.

[45] G. Rizzo, J. Gropper, M. Piollet, E. Vafadarnejad, A. Rizakou, S.R. Bandi, et al., Dynamics of monocyte-derived macrophage diversity in experimental myocardial infarction, Cardiovasc. Res. 119 (2023) 772–785, https://doi.org/10.1093/cvr/cvac113.

[46] A. Gainullina, D.A. Mogilenko, L.H. Huang, H. Todorov, V. Narang, K.W. Kim, et al., Network analysis of large-scale ImmGen and Tabula Muris datasets highlights metabolic diversity of tissue mononuclear phagocytes, Cell Rep. 42 (2023), https://doi.org/10.1016/j.celrep.2023.112046.

[47] E.H. Puttock, E.J. Tyler, M. Manni, E. Maniati, C. Butterworth, M. Burger Ramos, et al., Extracellular matrix educates an immunoregulatory tumor macrophage phenotype found in ovarian cancer metastasis, Nat. Commun. 14 (2023), https://doi.org/10.1038/s41467-023-38093-5.

[48] D. Ribatti, A revisited concept: contact inhibition of growth. From cell biology to malignancy, Exp. Cell Res. 359 (2017) 17–19, https://doi.org/10.1016/j.yexcr.2017.06.012.

[49] K. Mussar, A. Tucker, L. McLennan, A. Gearhart, A.J. Jimenez-Caliani, V. Cirulli, et al., Macrophage/epithelium cross-talk regulates cell cycle progression and migration in pancreatic progenitors, PLoS One 9 (2014), https://doi.org/10.1371/journal.pone.0089492.

[50] H. Lee, E. Abston, D. Zhang, A. Rai, Y. Jin, Extracellular vesicle: an emerging mediator of intercellular crosstalk in lung inflammation and injury, Front. Immunol. 9 (2018), https://doi.org/10.3389/fimmu.2018.00924.

[51] A. Beckmann, N. Hainz, T. Tschernig, C. Meier, Facets of communication: gap junction ultrastructure and function in cancer stem cells and tumor cells, Cancers 11 (2019), https://doi.org/10.3390/cancers11030288.

[52] J.I. Wu, L.H. Wang, Emerging roles of gap junction proteins connexins in cancer metastasis, chemoresistance and clinical application, J. Biomed. Sci. 26 (2019), https://doi.org/10.1186/s12929-019-0497-x.

[53] D.P. Wu, Y. Zhou, L.X. Hou, X.X. Zhu, W. Yi, S.M. Yang, et al., Cx43 deficiency confers emt-mediated tamoxifen resistance to breast cancer via c-src/pi3k/akt pathway, Int. J. Biol. Sci. 17 (2021) 2380–2398, https://doi.org/10.7150/ijbs.55453.

[54] M. Zhou, M. Zheng, X. Zhou, S. Tian, X. Yang, Y. Ning, et al., The roles of connexins and gap junctions in the progression of cancer, Cell Commun. Signal. 21 (2023), https://doi.org/10.1186/s12964-022-01009-9.

[55] X. Li, M. Tang, Exosomes released from M2 macrophages transfer miR-221-3p contributed to EOC progression through targeting CDKN1B, Cancer Med. 9 (2020) 5976–5988, https://doi.org/10.1002/cam4.3252.

[56] L.M. Hegarty, G.R. Jones, C.C. Bain, Macrophages in intestinal homeostasis and inflammatory bowel disease, Nat. Rev. Gastroenterol. Hepatol. 20 (2023) 538–553, https://doi.org/10.1038/s41575-023-00769-0.

[57] C. Cosentino, R. Regazzi, Crosstalk between macrophages and pancreatic β-cells in islet development, homeostasis and disease, Int. J. Mol. Sci. 22 (2021) 1–16, https://doi.org/10.3390/ijms22041765.

[58] A.M. Wen, K.L. Lee, I. Yildiz, M.A. Bruckman, S. Shukla, N.F. Steinmetz, Viral nanoparticles for in vivo tumor imaging, JoVE e4352 (2012), 10.3791/4352.

[59] H. Shirahama, B.H. Lee, L.P. Tan, N.J. Cho, Precise tuning of facile one-pot gelatin methacryloyl (GelMA) synthesis, Sci. Rep. 6 (2016), https://doi.org/10.1038/srep31036.

[60] J. Liu, K. Miller, X. Ma, S. Dewan, N. Lawrence, G. Whang, et al., Direct 3D bioprinting of cardiac micro-tissues mimicking native myocardium, Biomaterials 256 (2020), https://doi.org/10.1016/j.biomaterials.2020.120204.